

Low-temperature resistivity plateau and large magnetoresistance in compensated semimetal LaSbTe

Ratnadwip Singha, Biswarup Satpati, Prabhat Mandal

Saha Institute of Nuclear Physics, HBNI, 1/AF Bidhannagar, Calcutta 700 064, India

(Dated: September 30, 2016)

In this report, we present the magnetotransport properties of LaSbTe single crystals. With application of magnetic field, resistivity exhibits a prominent turn-on behavior followed by a plateau at low temperature. By adopting both metal-semiconductor crossover and Kohler scaling analysis, we have discussed the possible origin of the temperature dependence of resistivity. At 2 K and 9 T, a large, non-saturating transverse magnetoresistance (MR) $\sim 5 \times 10^3$ % has been observed. By rotating the magnetic field along different crystallographic directions, a large anisotropy is observed in MR, which indicates the anisotropic nature of the Fermi surface of LaSbTe. The non-linear field dependence of Hall resistivity confirms the presence of two types of charge carriers. From the semiclassical two-band fitting of Hall conductivity, very high carrier mobilities and almost equal electron and hole densities have been deduced, which results in the large MR in LaSbTe.

The complex interplay between electronic band structure and Fermi surface in condensed matter systems has always fascinated researchers as it leads to unique states of matter often reflected in their unusual electronic transport properties. In this regard, the recent discovery of topological insulator (TI) and three-dimensional topological semimetal (TSM) has emerged as a major boost, which has unfolded a whole new domain to explore the dynamics of relativistic particle in low-energy electronic system. Though TI was first realized experimentally [1–3], it is the three-dimensional TSM which has attracted much more attention due to the discovery of relativistic Dirac and Weyl fermions as quasi particle excitations in their symmetry protected semimetallic bulk state. Among the first TSM candidates, Cd_3As_2 and Na_3Bi were theoretically predicted [4, 5] and experimentally verified [6, 7] to host Dirac fermions, whereas Weyl fermions were identified in TX ($T = \text{Ta, Nb}$; $X = \text{As, P}$) family of materials [8–13]. Apart from the perspective of fundamental physics, the magnetotransport properties of these systems are of particular interest. Unique transport responses such as extreme magnetoresistance (XMR), ultrahigh electronic mobility and low carrier effective mass, make these materials highly preferable for technological applications. Therefore, prediction and experimental finding of new materials with topological non-trivial electronic band structure are of growing interest.

Recently, from band structure calculations, Xu *et al.* [14] have proposed that the members of the family WHM (W being Zr, Hf or La; H is from group IV or V; M is group VI element) are potential candidates for two-dimensional (2D) TI. Angle-resolved photoemission spectroscopy (ARPES) has revealed 2D topological insulating state in ZrSnTe [15], whereas several other members, ZrSiS , ZrSiSe and ZrSiTe have been confirmed as topological nodal line semimetals from ARPES and transport experiments [16–18]. Therefore, details studies on different members of this family are required, which may lead to novel quantum states of matter. In this

report, we present the magnetotransport properties of single crystalline LaSbTe, a member of the WHM family. Our experimental results reveal compensated semimetallic state along with very high carrier mobility, characteristic of TSMs. Magnetic field-induced resistivity upturn and large anisotropic MR have been observed, which have been analyzed both from the viewpoints of possible metal-semiconductor transition and Kohler scaling.

The single crystals of LaSbTe were grown by molten-salt flux method [19]. A mixture of LiCl (Alfa Aesar 99.9%) and RbCl (Alfa Aesar 99.8%) in 55:45 molar ratio was used as flux. The chloride salt mixture along with stoichiometric amount of La (Alfa Aesar 99.9%), Sb (Alfa Aesar 99.9999%) and Te (Alfa Aesar 99.999%) were taken in an alumina crucible which was then sealed in a quartz tube under vacuum. The quartz tube was heated to 700°C and kept at this temperature for 5 days. After that, the furnace was cooled slowly (2°C/h) to room temperature. Shiny single crystals were obtained which were washed with water to remove the chloride salt and cleaned with acetone. X-ray diffraction (XRD) patterns were obtained in a Rigaku X ray diffractometer (TTRAX II). High resolution transmission electron microscopy (HRTEM) of the crystals were done in FEI, TECNAI G² F30, S - TWIN microscope operating at 300 kV and equipped with GATAN Orius SC1000B CCD camera. Transport measurements were performed in a 9 T PPMS (Quantum Design) with ac transport option on several single crystal samples from the same batch, all shaped into thin rectangular bar geometry.

In the inset of Fig. 1(a), a single crystal of LaSbTe of typical dimensions 2 mm×1 mm×0.6 mm is shown with different crystallographic axes along which measurements have been done. The XRD pattern of powdered single crystals is illustrated in Fig. 1(a). The sharp diffraction peak with small full-width at half-maximum confirms the high quality of the grown crystals. LaSbTe crystallizes in a ZrSiS type structure

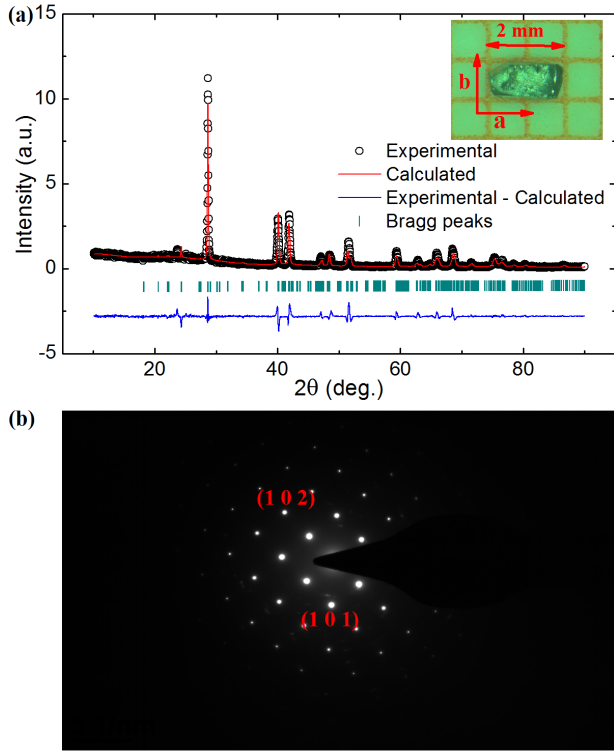


FIG. 1. (a) Powder XRD pattern of the LaSbTe single crystals. Inset shows a typical single crystal. (b) SAED pattern obtained in HRTEM measurement.

and belongs to orthorhombic space group $Pmcn$ [19, 20]. The refined lattice parameters calculated from XRD spectra, $\mathbf{a}=4.39037$, $\mathbf{b}=4.42935$ and $\mathbf{c}=19.48580$ Å, are consistent with previous report [19]. The selective area electron diffraction (SAED) pattern obtained in HRTEM is shown in Fig. 1(b) with the Miller indices of the corresponding lattice planes.

In Fig. 2(a), the resistivity of two samples from the same batch is shown as a function of temperature. Both the samples exhibit identical temperature dependence, decreasing almost linearly from 300 K and showing weak temperature dependence below 30 K. The resistivity at 2 K is as low as $\sim 9 \mu\Omega \text{ cm}$ for sample 1 and $\sim 6 \mu\Omega \text{ cm}$ for sample 2, which are comparable to that reported in Dirac semimetal Cd_3As_2 and Weyl semimetal candidates TaAs, NbP and TaP [10, 13, 21, 22]. The calculated residual resistivity ratio $[\text{RRR}=\rho_{xx}(300 \text{ K})/\rho_{xx}(2 \text{ K})]$ for both the samples (sample 1 ~ 8.4 ; sample 2 ~ 14), suggests good metallicity of the grown LaSbTe crystals. For both the crystals, the low-temperature resistivity can be fitted well [Fig. 2(a) inset] using $\rho_{xx}(T) = A + BT^n$ type relation with $n \sim 3$, where A and B are constants. Deviation from a value $n=2$ is generally considered as a departure from the pure electronic correlation dominated scattering mechanism [23]. Similar type of temperature dependence of resistivity has also been observed in unconventional

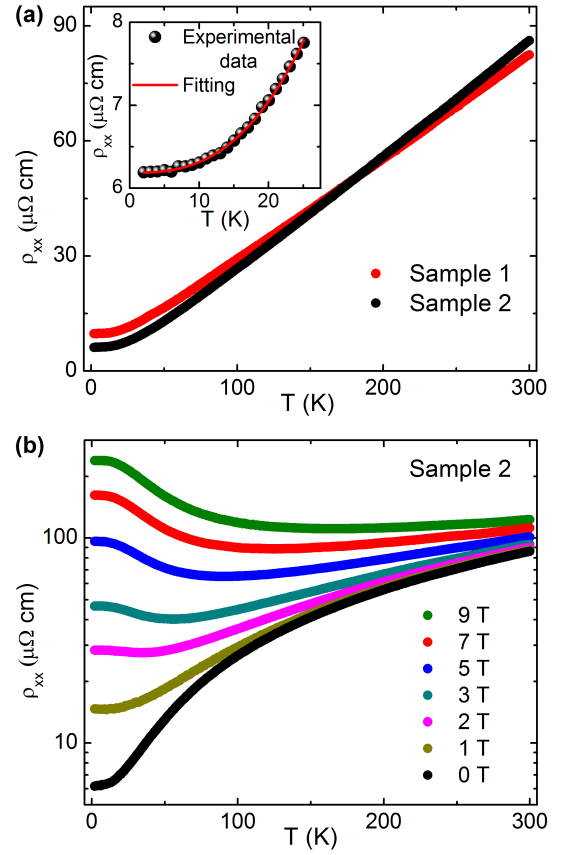


FIG. 2. (a) Temperature dependence of resistivity for two samples from the same batch. Inset shows the low temperature region fitted with $\rho_{xx}(T) = A + BT^n$. (b) $\rho_{xx}(T)$ under different transverse magnetic field strengths.

semimetals LaSb ($n=4$) and LaBi ($n=3$), elemental yttrium and transition metal carbide and has been attributed to interband electron-phonon scattering [24–27].

When a magnetic field is applied, resistivity is observed to increase rapidly, particularly in the low-temperature region [Fig. 2(b)]. Above a critical magnetic field ~ 1 T, the resistive behavior of LaSbTe at low temperatures modifies significantly. The nature of the slope of the $\rho_{xx}(T)$ curve changes and a metal-semiconductor like crossover appears. Similar upturn in low-temperature resistivity has been observed in several TSMs [13, 21, 24, 25]. In analogy to dynamical chiral symmetry breaking in relativistic theories of the $(2 + 1)$ -dimensional Dirac fermions, Khveshchenko proposed that this type of magnetic field-induced crossover is due to the gap opening at the band crossing points [28]. However, subsequent explanations in terms of scaling analysis, have also been proposed [29–31]. Here, we have adopted both the approaches to discuss the resistivity turn-on behavior in LaSbTe. $\rho_{xx}(T)$ can be analyzed considering the thermal activated transport, $\rho_{xx}(T) \propto \exp(E_g/k_B T)$, as in the case of intrinsic semiconductor and several topological semimetal systems

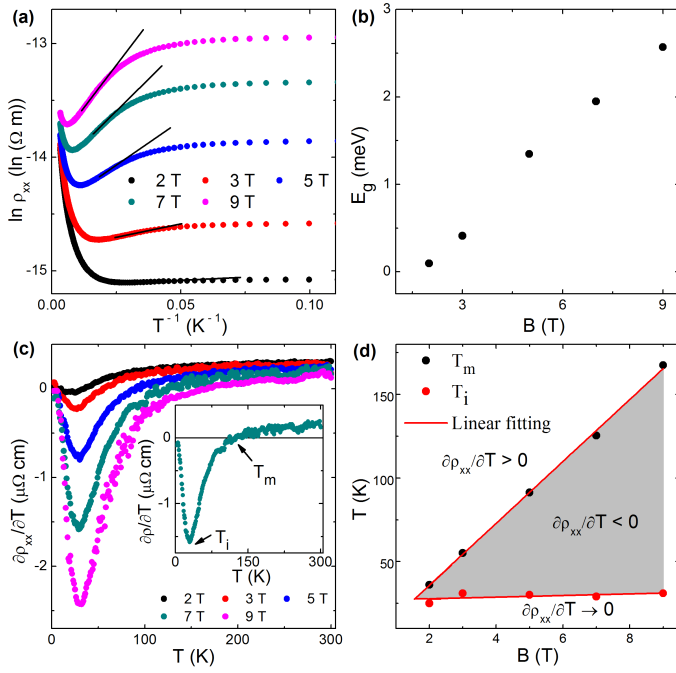


FIG. 3. (a) $\ln \rho$ plotted as a function of T^{-1} . (b) Field dependence of the calculated thermal activation energy gap. (c) $\partial \rho_{xx}/\partial T$ plotted as a function of temperature for different applied field strengths. Inset shows the crossover temperature (T_m) and plateau temperature (T_i) for 7 T. (d) Triangular temperature-field phase diagram constructed from T_m and T_i .

[24, 32]. In Fig. 3(a), we have plotted $\ln \rho_{xx}$ as a function of T^{-1} . From the slope of the curve, the thermal activation energy gap (E_g) ~ 2.6 meV has been calculated at 9 T, which is quite small. As shown in Fig. 3(b), the calculated energy gap clearly shows a strong magnetic field dependence.

Above the critical magnetic field, the crossover in $\rho_{xx}(T)$ curve is followed by a plateau at low temperatures. Though, the field-induced resistivity plateau has been observed in several topologically non-trivial semimetallic systems [13, 21, 24, 25, 31], its origin is not yet settled unambiguously. Very similar temperature-dependent resistivity has been observed in topological insulators $\text{Bi}_2\text{Te}_2\text{Se}$ and SmB_6 in absence of magnetic field, where the low-temperature resistivity saturation arises from the time-reversal symmetry (TRS) protected conducting surface state [33, 34]. On the other hand, the field-induced resistivity plateau in LaSbTe appears due to the break down of TRS. In Fig. 3(c), the first-order derivative of the resistivity $\partial \rho_{xx}/\partial T$ is plotted as a function of temperature for different magnetic field strengths. As shown in the inset, from the resultant curves, two distinct characteristic temperatures can be identified, the crossover temperature T_m , where $\partial \rho_{xx}/\partial T$ changes sign and T_i , below which the resistivity plateau starts to appear. While T_m increases monotonically with field, T_i is almost field independent. In Fig.

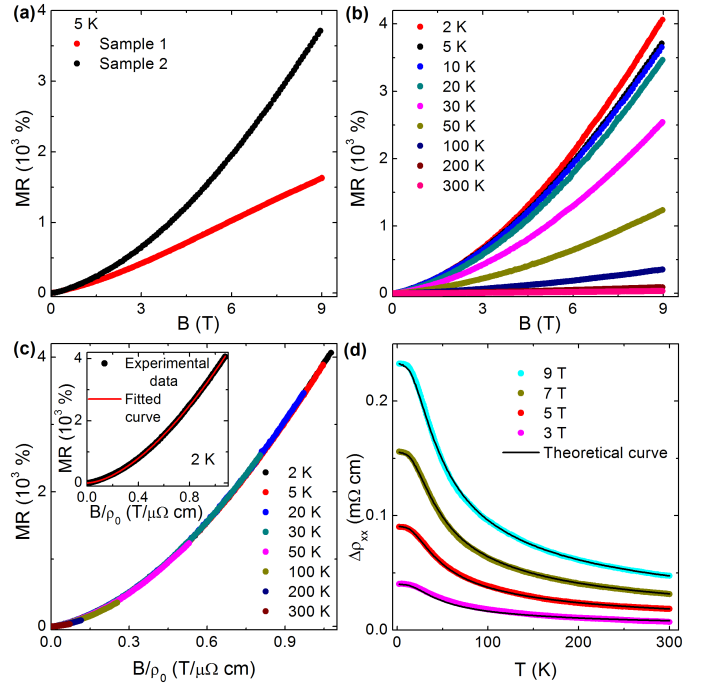


FIG. 4. (a) Transverse MR for sample 1 and sample 2. (b) Transverse MR for sample 2 at different representative temperatures. (c) MR at different temperatures are scaled using Kohler's rule. Inset shows the power-law (Eq. 1) fitting of the experimental data. (d) Field-dependent part of $\rho_{xx}(T)$. Solid lines denote the generated curves from Kohler's rule.

3(d), following the approach of Tafti *et al.* [35], we have constructed a triangular temperature-field phase diagram for LaSbTe by plotting T_m and T_i as a function of magnetic field. This triangular phase diagram has been seen to be universal for all semimetallic systems showing extreme magnetoresistance (XMR) [35]. In the figure, the gray shaded area which corresponds to $\partial \rho_{xx}/\partial T < 0$, denotes the region where XMR occurs. The linear fitted curves of $T_m(B)$ and $T_i(B)$ merge at $B_0 \sim 1.6$ T, which is precisely the turn-on field above which metal-semiconductor like crossover appears. The region above the shaded triangle with $\partial \rho_{xx}/\partial T > 0$ is of metallic conduction and negligible MR, whereas the area below the shaded triangle denotes the plateau region ($\partial \rho_{xx}/\partial T \rightarrow 0$). As has been shown in bismuth and graphite [29], the triangular region in the temperature-field phase diagram can be specified by the inequality, $\hbar/\tau \lesssim \hbar\omega_c \lesssim k_B T$, where τ is the electron-phonon scattering time and ω_c is the cyclotron frequency. In clean semimetals with low carrier density, $\tau^{-1} \ll k_B T/\hbar$ and hence, there exists a wide temperature-field range where XMR and metal-semiconductor like crossover in resistivity appear. On the other hand, large carrier density and strong impurity scattering, limit the MR in conventional metals [36].

Next, we measure the transverse MR, i.e., MR under

transverse electric and magnetic fields. In Fig. 4(a), the MR of two samples is compared at 5 K with current along **a** and field along **c** axis. It is clear from figure that the sample with higher RRR (sample 2) shows stronger response to magnetic field than the other one (sample 1). Therefore, the value of MR clearly depends on the sample quality. However, the MR for both the samples is observed to follow same power-law behavior, $MR \propto B^m$ with $m \sim 1.6$. In Fig. 4(b), we have plotted MR for sample 2 as a representative, at different temperatures. At 2 K and 9 T, a large MR $\sim 4 \times 10^3$ % is obtained without any signature of saturation. Though the observed MR is not among the largest reported so far, it is comparable to several topological semimetal candidates [22, 37–39]. With the increase in temperature, however, the MR decreases rapidly to only ~ 35 % at 300 K and 9 T. As shown in Fig. 4(c), employing the Kohler's rule,

$$MR = \alpha(B/\rho_0)^m \quad (1)$$

with $\alpha = 4.8 \times 10^{-9} (\Omega \text{ cm/T})^{1.6}$ and $m = 1.6$, the MR curves at different temperatures can be scaled to a single curve. According to semiclassical two-band theory, the validity of Kohler rule with $MR \propto (B/\rho_0)^2$ suggests a perfectly compensated system [23]. In LaSbTe, however, the exponent is not exactly 2 and a small but detectable deviation from scaling in Fig. 4(c) is observed. This indicates that the densities and or the temperature dependence of mobility are not completely identical for two types of carriers revealed from the Hall measurement which we discuss later [31, 40]. Adopting a modified form of Eq. (1),

$$\rho_{xx}(B) = \rho_0 + \alpha B^m / \rho_0^{m-1} \quad (2)$$

it can be shown that the resistivity in a magnetic field consists of two components, zero-field resistivity ρ_0 and field-induced component $\Delta\rho_{xx} = \alpha B^m / \rho_0^{m-1}$. The competition between these two terms may give rise the observed minimum in the temperature dependence of resistivity above the critical field. In Fig. 4(d), the field induced resistivity component is plotted for different magnetic fields. As illustrated by the solid lines, the experimental data at all magnetic fields can be described well by Eq. (2) with $\alpha = 4.8 \times 10^{-9} (\Omega \text{ cm/T})^{1.6}$ and $m = 1.6$. MR at different magnetic fields in fact collapses onto a single curve when normalized by their respective values at 2 K (Fig. 5(a)). This suggests that the temperature dependence of MR remains same for all magnetic fields. On the other hand, the calculated thermal activation energy gap (E_g) has been observe to increase monotonically with field. So, sharper metal-semiconductor like crossover is expected at higher magnetic fields. Therefore, the validity of such scaling behavior, seems to be contradictory to the picture of possible field-induced gap at the band crossing points. As α and m are temperature-independent constants, Eq. (2) suggests that the temperature dependence of $\Delta\rho_{xx}$ is determined entirely by $\rho_0(T)$, which is

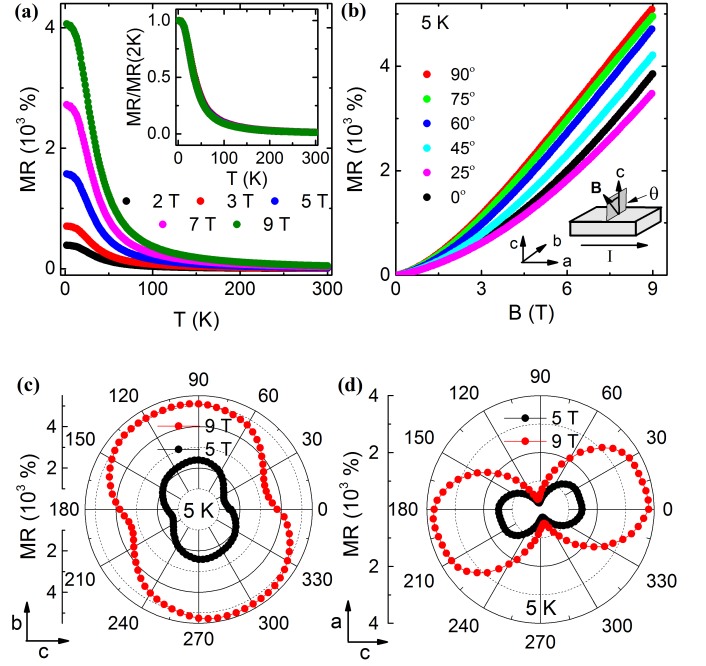


FIG. 5. (a) Temperature dependence of MR. Inset shows the normalized MR with the value at 2 K. (b) MR as a function of magnetic field at 5 K when B is tilted along different crystallographic directions. Inset shows the schematic of the experimental setup. (c) Polar plot of TMR for two different field strengths with current along **a** axis and magnetic field rotated in the **bc** plane. (d) Angular dependence of MR with current parallel to **a** axis and field rotated in the **ac** plane.

again inversely proportional to density and mobility of the charge carrier. Therefore, in a system where carrier density remains constant with temperature, the resistivity turn-on behavior results from strong temperature dependence of the carrier mobility [29, 31]. In spite of being conflicting, both metal-semiconductor crossover [24, 32] and Kohler scaling analysis [29–31] can distinctly explain the observed transport behavior to a great extent and are used simultaneously. However, the actual origin remains an open question, which is yet to be answered decisively.

For in depth understanding of magnetotransport properties of LaSbTe, we have measured the MR by tilting the magnetic field along different crystallographic directions while keeping the current direction unaltered. The experimental configuration is shown schematically in the inset of Fig. 5(b) with current along **a** axis and magnetic field is rotated within the **bc** plane. As we increase the angle (θ) from 0° to 25° , MR is seen to decrease and then increases with further increase of θ . Maximum MR $\sim 5 \times 10^3$ is recorded at $\theta \sim 90^\circ$ (**B**||**b**). In Fig. 5(c), MR for two different field strengths, is plotted as a function of the tilting angle. The resultant curve possesses a two-fold rotational symmetry, indicating a strong directional dependence and hence a significant

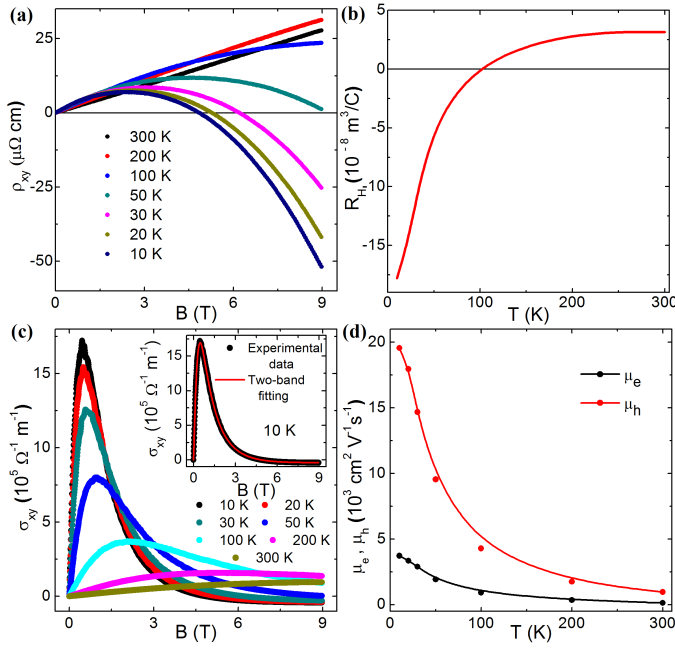


FIG. 6. (a) Field dependence of Hall resistivity at different temperatures. (b) Temperature dependence of Hall coefficient obtained from the slopes of ρ_{xy} curves in high field region. At about 100 K, the Hall coefficient changes sign from positive to negative. (c) The Hall conductivity plotted as a function magnetic field. Inset shows the two-band fitting of the Hall conductivity at 10 K. (d) Temperature dependence of electron and hole carrier mobility obtained from two-band fitting.

anisotropy in the Fermi surface topology of LaSbTe. The large anisotropic MR has also been observed in other members of the *WHM* family [17, 18], originated from the quasi two-dimensional nature of the Fermi surface [16].

We have also measured the MR with current along **a** axis and magnetic field is rotated within the **ac** plane. As shown in the Fig. 5(d), MR becomes minimum when electric and magnetic fields are parallel to each other ($\theta=90^\circ$; $\mathbf{B}\parallel\mathbf{a}$), which is expected due to the absence of Lorentz force in such a configuration. MR increases monotonically as the angle between **E** and **B** increases.

To determine the nature and density of the charge carriers, we have performed the Hall effect measurement in the temperature range 10-300 K. In Fig. 6(a), the measured Hall resistivity (ρ_{xy}) is plotted as a function of magnetic field. At 300 K, ρ_{xy} is found to be almost linear and positive which indicate hole-dominated charge conduction. However, with decreasing temperature, $\rho_{xy}(B)$ becomes sublinear and, around 100 K, its sign changes from positive to negative at high fields. The magnetic

field dependence of ρ_{xy} clearly shows that more than one type of charge carrier is present in LaSbTe. From the high-field slope of the $\rho_{xy}(B)$ curves, the Hall coefficient has been determined and shown in Fig. 6(b) as a function of temperature. Following the semiclassical two-band model [41], we have fitted the Hall conductivity σ_{xy} in Fig. 6(c) using,

$$\sigma_{xy} = [n_h \mu_h^2 \frac{1}{1 + (n_h B)^2} - n_e \mu_e^2 \frac{1}{1 + (n_e B)^2}] \quad (3)$$

where $\sigma_{xy} = \frac{\rho_{xy}}{\rho_{xy}^2 + \rho_{xx}^2}$, ρ_{xx} being the longitudinal resistivity. n_e (n_h) and μ_e (μ_h) are electron (hole) density and mobility, respectively. From the fitting parameters, the electron and hole densities at 10 K are found to be, $1.53 \times 10^{19} \text{ cm}^{-3}$ and $1.17 \times 10^{19} \text{ cm}^{-3}$ respectively, which indicate almost perfect electron-hole carrier compensation in LaSbTe. The obtained electron and hole mobilities are large and at 10 K are $\sim 3.7 \times 10^3 \text{ cm}^2 \text{ V}^{-1} \text{ s}^{-1}$ and $\sim 1.9 \times 10^4 \text{ cm}^2 \text{ V}^{-1} \text{ s}^{-1}$ respectively, which are comparable to the carrier mobility in Dirac semimetals Cd_3As_2 , ZrTe_5 , TlBiSSe and Weyl semimetal WTe_2 [37, 42–44]. As shown in Fig. 6(d), the mobility for both types of carriers decreases as the temperature increases.

In conclusion, we present the systematic study of magnetotransport properties of single crystalline LaSbTe. Magnetic field-induced resistivity turn-on along with low-temperature resistivity plateau have been observed and analyzed from the aspects of possible metal-semiconductor crossover as well as the Kohler's scaling. From the $\rho_{xx}(T)$ curves, a triangular temperature-field phase diagram has been constructed, which is universal for semimetals showing XMR. At 2 K and 9 T, a large transverse MR $\sim 5 \times 10^3 \%$ has been observed without any signature of saturation. By rotating the magnetic field along different crystallographic directions, significant anisotropy in the magnetotransport properties has been observed which implies an anisotropic Fermi surface in LaSbTe. From the Hall measurement, the presence of two types of carriers is confirmed. The semiclassical two-band fitting of the Hall conductivity reveals almost perfect carrier compensation with very high carrier mobilities and explains the large MR in electron-hole resonance regime. As LaSbTe represents a large family of materials with identical electronic band structure and proposed as potential candidate for two-dimensional TI, this study may stimulate further interest in the present system as well as other members of the family.

We acknowledge and thank A. Pariari, S. Pakhira, G. Bhattacharjee and S. Roy for their help during measurements and fruitful discussions.

- Bansil, D. Grauer, Y. S. Hor, R. J. Cava, M. Z. Hasan, Nat. Phys. **5**, 398 (2009).
- [3] Y. L. Chen, J. G. Analytis, J.-H. Chu, Z. K. Liu, S.-K. Mo, X. L. Qi, H. J. Zhang, D. H. Lu, X. Dai, Z. Fang, S. C. Zhang, I. R. Fisher, Z. Hussain, Z.-X. Shen, Science **325**, 178 (2009).
- [4] Z. Wang, Y. Sun, X.-Q. Chen, C. Franchini, G. Xu, H. Weng, X. Dai, Z. Fang, Phys. Rev. B **85**, 195320 (2012).
- [5] Z. Wang, H. Weng, Q. Wu, X. Dai, Z. Fang, Phys. Rev. B **88**, 125427 (2013).
- [6] Z. K. Liu, J. Jiang, B. Zhou, Z. J. Wang, Y. Zhang, H. M. Weng, D. Prabhakaran, S.-K. Mo, H. Peng, P. Dudin, T. Kim, M. Hoesch, Z. Fang, X. Dai, Z. X. Shen, D. L. Feng, Z. Hussain, Y. L. Chen, Nat. Mat. **13**, 677 (2014).
- [7] Z. K. Liu, B. Zhou, Y. Zhang, Z. J. Wang, H. M. Weng, D. Prabhakaran, S.-K. Mo, Z. X. Shen, Z. Fang, X. Dai, Z. Hussain, Y. L. Chen, Science **343**, 864 (2014).
- [8] H. Weng, C. Fang, Z. Fang, B. A. Bernevig, X. Dai, Phys. Rev. X **5**, 011029 (2015).
- [9] S.-Y. Xu, I. Belopolski, N. Alidoust, M. Neupane, G. Bian, C. Zhang, R. Sankar, G. Chang, Z. Yuan, C.-C. Lee, S.-M. Huang, H. Zheng, J. Ma, D. S. Sanchez, B. K. Wang, A. Bansil, F. Chou, P. P. Shibaev, H. Lin, S. Jia, M. Z. Hasan, Science **349**, 613 (2015).
- [10] X. Huang, L. Zhao, Y. Long, P. Wang, D. Chen, Z. Yang, H. Liang, M. Xue, H. Weng, Z. Fang, X. Dai, G. Chen, Phys. Rev. X **5**, 031023 (2015).
- [11] S.-Y. Xu, I. Belopolski, D. S. Sanchez, C. Zhang, G. Chang, C. Guo, G. Bian, Z. Yuan, H. Lu, T.-R. Chang, P. P. Shibaev, M. L. Prokopovych, N. Alidoust, H. Zheng, C.-C. Lee, S.-M. Huang, R. Sankar, F. Chou, C.-H. Hsu, H.-T. Jeng, A. Bansil, T. Neupert, V. N. Strocov, H. Lin, S. Jia, M. Z. Hasan, Science Adv. **1**, 1501092 (2015).
- [12] S.-Y. Xu, N. Alidoust, I. Belopolski, Z. Yuan, G. Bian, T.-R. Chang, H. Zheng, V. N. Strocov, D. S. Sanchez, G. Chang, C. Zhang, D. Mou, Y. Wu, L. Huang, C.-C. Lee, S.-M. Huang, B. Wang, A. Bansil, H.-T. Jeng, T. Neupert, A. Kaminski, H. Lin, S. Jia, M. Z. Hasan, Nat. Phys. **11**, 748 (2015).
- [13] C. Shekhar, A. K. Nayak, Y. Sun, M. Schmidt, M. Nicklas, I. Leermakers, U. Zeitler, Y. Skourski, J. Wosnitza, Z. Liu, Y. Chen, W. Schnelle, H. Borrmann, Y. Grin, C. Felser, B. Yan, Nat. Phys. **11**, 645 (2015).
- [14] Q. Xu, Z. Song, S. Nie, H. Weng, Z. Fang, X. Dai, Phys. Rev. B **92**, 205310 (2015).
- [15] R. Lou, J.-Z. Ma, Q.-N. Xu, B.-B. Fu, L.-Y. Kong, Y.-G. Shi, P. Richard, H.-M. Weng, Z. Fang, S.-S. Sun, Q. Wang, H.-C. Lei, T. Qian, H. Ding, S.-C. Wang, Phys. Rev. B **93**, 241104(R) (2016).
- [16] L. M. Schoop, M. N. Ali, C. Straßer, A. Topp, A. Varykhalov, D. Marchenko, V. Duppel, S. S. P. Parkin, B. V. Lotsch, C. R. Ast, Nat. Commun. **7**, 11696 (2016).
- [17] R. Singha, A. Pariari, B. Satpati, P. Mandal, arXiv:1602.01993v2.
- [18] J. Hu, Z. Tang, J. Liu, X. Liu, Y. Zhu, D. Graf, K. Myhro, S. Tran, C. N. Lau, J. Wei, Z. Mao, Phys. Rev. Lett. **117**, 016602 (2016).
- [19] E. DiMasi, B. Foran, M. C. Aronson, S. Lee, Phys. Rev. B **54**, 13587 (1996).
- [20] C. Wang, T. Hughbanks, Inorg. Chem. **34**, 5524 (1995).
- [21] J. Hu, J. Y. Liu, D. Graf, S. M. A. Radmanesh, D. J. Adams, A. Chuang, Y. Wang, I. Chiorescu, J. Wei, L. Spinu, Z. Q. Mao, Sci. Rep. **6**, 18674 (2016).
- [22] Z. J. Xiang, D. Zhao, Z. Jin, C. Shang, L. K. Ma, G. J. Ye, B. Lei, T. Wu, Z. C. Xia, X. H. Chen, Phys. Rev. Lett. **115**, 226401 (2015).
- [23] J. M. Ziman, *Electrons and Phonons: The Theory of Transport Phenomena in Solids*, Classics Series, Oxford University Press, New York (2001).
- [24] F. F. Tafti, Q. D. Gibson, S. K. Kushwaha, N. Haldolaarachchige, R. J. Cava, Nat. Phys. **12**, 272 (2016).
- [25] S. Sun, Q. Wang, P.-J. Guo, K. Liu, H. Lei, New J. Phys. **18**, 082002 (2016).
- [26] P. M. Hall, S. Legvold, F. H. Spedding, Phys. Rev. **116**, 1447 (1959).
- [27] X. Zhang, Z. Xiao, H. Lei, Y. Toda, S. Matsuishi, T. Kamiya, S. Ueda, H. Hosono, Chem. Mater. **26**, 6638 (2014).
- [28] D. V. Khvashchenko, Phys. Rev. Lett. **87**, 206401 (2001).
- [29] X. Du, S.-W. Tsai, D. L. Maslov, A. F. Hebard, Phys. Rev. Lett. **94**, 166601 (2005).
- [30] Y. Kopelevich, J. C. M. Pantoja, R. R. da Silva, S. Moehlecke, Phys. Rev. B **73**, 165128 (2006).
- [31] Y. L. Wang, L. R. Thoutam, Z. L. Xiao, J. Hu, S. Das, Z. Q. Mao, J. Wei, R. Divan, A. Luican-Mayer, G. W. Crabtree, W. K. Kwok, Phys. Rev. B **92**, 180402(R) (2015).
- [32] Y.-Y. Wang, Q.-H. Yu, P.-J. Guo, K. Liu, T.-L. Xia, Phys. Rev. B **94**, 041103(R) (2016).
- [33] Z. Ren, A. A. Taskin, S. Sasaki, K. Segawa, Y. Ando, Phys. Rev. B **82**, 241306(R) (2010).
- [34] D. J. Kim, S. Thomas, T. Grant, J. Botimer, Z. Fisk, Jing Xia, Sci. Rep. **3**, 3150 (2013).
- [35] F. F. Tafti, Q. Gibson, S. Kushwaha, J. W. Krizan, N. Haldolaarachchige, R. J. Cava, Proc. Natl. Acad. Sci. **113**, 3475 (2016).
- [36] A. A. Abrikosov, *Fundamentals of the Theory of metals*, North-Holland, Amsterdam (1988).
- [37] M. Novak, S. Sasaki, K. Segawa, Y. Ando, Phys. Rev. B **91**, 041203(R) (2015).
- [38] N. Wakeham, E. D. Bauer, M. Neupane, F. Ronning, Phys. Rev. B **93**, 205152 (2016).
- [39] Orest Pavlosiuk, Przemyslaw Swatek, Piotr Wisniewski, arXiv:1604.06945v2.
- [40] R. H. McKenzie, J. S. Qualls, S. Y. Han, J. S. Brooks, Phys. Rev. B **57**, 11854 (1998).
- [41] C. M. Hurd, *The Hall effect in metals and alloys*, Plenum Press, New York (1972).
- [42] A. Narayanan, M. D. Watson, S. F. Blake, N. Bruyant, L. Drigo, Y. L. Chen, D. Prabhakaran, B. Yan, C. Felser, T. Kong, P. C. Canfield, A. I. Coldea, Phys. Rev. Lett. **114**, 117201 (2015).
- [43] G. Zheng, J. Lu, X. Zhu, W. Ning, Y. Han, H. Zhang, J. Zhang, C. Xi, J. Yang, H. Du, K. Yang, Y. Zhang, M. Tian, Phys. Rev. B **93**, 115414 (2016).
- [44] Y. Luo, H. Li, Y. M. Dai, H. Miao, Y. G. Shi, H. Ding, A. J. Taylor, D. A. Yarotski, R. P. Prasankumar, J. D. Thompson, App. Phys. Lett. **107**, 182411 (2015).